Original article

Capillary and viscous forces during CO_2 flooding in tight reservoirs

Chuanbao Zhang[1], Qingfu Zhang[1], Wendong Wang[2,3]*, Qiuheng Xie[2,3], Yuliang Su[2,3], Atif Zafar[4]

[1]*Exploration and Development Research Institute, Shengli Oilfield Company, SINOPEC, Dongying 257015, P. R. China*

[2]*Key Laboratory of Unconventional Oil & Gas Development, Ministry of Education, China University of Petroleum (East China), Qingdao 266580, P. R. China*

[3]*School of Petroleum Engineering, China University of Petroleum (East China), Qingdao 266580, P. R. China*

[4]*Department of Petroleum Technology, University of Karachi, University Road, Karachi 75270, Pakistan*

Abstract:
In this study, the multiphase multicomponent Shan-Chen lattice Boltzmann method is employed to analyze the impact of capillary force on oil-CO_2-water fluid flow and enhanced oil recovery. Various sizes of the single throat are designed to simulate the interaction between displacing and displaced phases as well as their mechanical equilibrium. Several sensitivities are taken into account, such as wettability, miscibility, interfacial tension, and pore aperture. Based on the objective reservoir conditions, supercritical CO_2 as an injection fluid is adopted to study the influence of different displacement patterns on the mechanical equilibrium in both homogenous and heterogeneous porous media, in which enhanced oil recovery is also quantitatively estimated. The results show that the water-alternating-gas injection pattern reduces the moving speed of the leading edge by increasing the swept area of the residual oil, and inhibits the breakthrough effect of the gas, making it the optimal displacement method in terms of the degree of oil production. Compared with the results of different displacement patterns, the enhanced oil recovery of water-alternating-gas injection is the highest, followed by supercritical CO_2 flooding after water flooding, and lastly, continuous supercritical CO_2 flooding.

1. Introduction

About 38% of international oil and gas reserves and about 46% of Chinese oil and gas reserves are dominated by low-permeability resource types. The effective development of these resources is of great strategic significance to ensure the sustainable development of Chinese oil and gas (Wang et al., 2007). Low-permeability reservoirs are rich in resources, widely distributed and comprise the main type of oil and gas reservoirs that need to be urgently developed. CO_2 injection has been increasingly used for enhanced oil recovery (EOR) in low-permeability reservoirs at home and abroad. It is the main technique for EOR in low-permeability reservoirs (Khosravi et al., 2014; Zhao et al., 2020). After CO_2 injection, processes such as dissolution (Tang and Morrow, 1999; Yousef et al., 2011), viscosity reduction and competitive adsorption will change the occurrence state and macroscopic properties of reservoir fluids, further affecting EOR. Mixed with crude oil, CO_2 can reduce the interfacial tension (IFT) between the fluids and the viscosity of oil, expand crude oil volume, extract hydrocarbon components in crude oil, and eventually improve flooding efficiency (Rao et al., 1992; Lansangan and Smith, 1993; Wei et al., 2020).

CO_2 injection is deemed one of the most effective and economic methods for EOR in conventional oil reservoirs and is therefore widely used in oil fields (Jarrell et al., 2002; Jensen et al., 2013; Tapia et al., 2016; Welkenhuysen et al., 2017; Jiang et al., 2019). It is not only beneficial

for alleviating the 'greenhouse effect' by CO_2 sequestration (Lackner, 2003; Xu et al., 2022; Zhang et al., 2022), but also for performing EOR in tight oil reservoirs (Wang et al., 2016). The properties of CO_2 make it readily miscible and flow together easily with oil through the porous media (Martin and Taber, 1992; Lambert et al., 1996). Furthermore, water-alternating-gas injection (WAG), which combines the advantages of both CO_2 flooding and water flooding, is the most prevailingly utilized method in EOR projects compared with miscible and immiscible continuous CO_2 flooding, water flooding, or huff and puff CO_2 injection (Christensen et al., 2001; Alvarado and Manrique, 2010); its EOR is higher than others by 5%-25% (Ghedan, 2009). Therefore, WAG should also be studied to improve its performance in oil fields. Recently, many studies focused on how CO_2 could reduce the capillary force resistance and the balance between capillary force and viscous force by using both experiments and simulations. A core experiment was carried out to explore the effect of the two forces on EOR (Nobakht et al., 2007). The phase behavior of the fluid mixture and the fluid transport process were integrated into a systematic method to analyze the effect of the capillary pressure (Zhang et al., 2017). Some flow behaviors exhibited in porous media were captured in an etched network, and the quantitative calculation and theoretical model were proposed (Lenormand et al., 1983). The viscous finger was observed by lattice Boltzmann (LB) simulation under an immiscible condition in porous media (Dong et al., 2011). In a single tortuous capillary, the influence of convolutedness of the capillary during the capillary rise process of wetting liquid was studied (Cai et al., 2010). A simulation was developed to study the problem of displacing a ganglion of a fluid by another immiscible one and predict the location of the ganglion with time (Salama et al., 2021). A comprehensive review of recent studies in mathematical models which modified and extended the Lucas-Washburn (LW) equation for various microchannels and porous media was summarized, and a review of the numerical simulations on the LW equation was also introduced (Cai et al., 2021). Using nuclear magnetic resonance technology, the fluid flow was captured on spontaneous imbibition (Zhou et al., 2022). Fluid displacements in the three-dimensional pore spaces of Berea sandstone were conducted by two-phase LB model for the factual conditions, and two dimensionless numbers were introduced to explain the flow behavior in the diagrams (Tsuji et al., 2016). A color LB model was used to simulate forced imbibition in three natural rocks at four different injection rates (Liu et al., 2022). A model of two-phase flow in the heterogenous wet porous media was investigated to analyse the impact of wettability on the capillary force and the displacement efficiency (Xiao et al., 2022). Several studies focused on the balance of capillary and viscous force impacting the performance of EOR quantitatively. However, the LB simulation is seldom performed by considering three-phase fluid flow during the flooding processes.

In this study, a three-phase simulation model based on the LB method is established, including a set of quantitative estimation methods, which can simulate the three-phase flow of oil, gas and water in porous media. The rationality of this
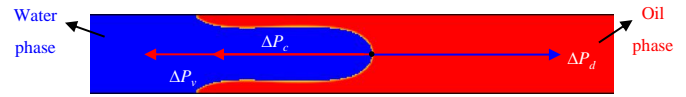

Fig. 1. Correlation diagram of the forces.

model is verified by evaluating contact angle and Laplace's law, and the mechanisms of water flooding, continuous CO_2 flooding, and CO_2 flooding after water flooding in single pores of different sizes are investigated. In addition, the model is used to study the EOR mechanism of continuous CO_2 flooding, CO_2 flooding after water flooding, and WAG. It is found that the three factors of IFT, oil-gas miscibility and wall wettability affect the fluid moving speed and EOR by various degrees.

2. Mathematical model and physical background

2.1 Governing equations

Herein, the process of different injection fluids (e.g., water or the supercritical CO_2 ($scCO_2$)) for EOR includes two or three phases of flow during the reservoir formation. For simplification, all of the fluids in this process are deemed incompressible fluids. The fluid flows through porous media without thermal transport and reactions, and the pore-scale continuity and momentum equations can be written as (Landau and Lifshits, 1959):

$$\nabla \cdot \mathbf{u} = 0 \tag{1}$$

$$\rho \frac{\partial \mathbf{u}}{\partial t} + \rho \mathbf{u} \cdot \nabla \mathbf{u} = -\nabla p + \rho v \nabla^2 \mathbf{u} \tag{2}$$

where ρ represents the density of the fluid, kg/m³; t represents time, s; $\mathbf{u}$ is the velocity vector, m/s; p denotes the pressure, Pa; v is the kinematic viscosity, m²/s.

2.2 Estimation of viscous force

When analyzing the balance between capillary force and viscous force during the displacement process, the total driving force ΔP_d remains unchanged, which is the sum of capillary force ΔP_c, oil phase viscous force and water phase viscous force ΔP_v, Pa, as shown in Eq. (3). Fig. 1 expresses Eq. (3) in the form of a diagram.

$$\Delta P_v = \Delta P_d - \Delta P_c \tag{3}$$

During the displacement process, both the displacing phase and displaced phase are subjected to the viscous force on flow. According to Eq. (3), the capillary force generated by IFT constitutes the total resistance, and the fluids (e.g., water, $scCO_2$, or oil) can flow against the resistance by exerting a total driving force on the displacing fluids.

The irregular interface between oil and water can be obtained from the oil-water distribution in the LB model. Due to the objective reservoir properties, a no-slip condition is considered herein. The exact value of the viscous and capillary forces is hard to estimate directly. Therefore, the no-slip Hagen-Poiseuille (HP) equation is used to fit the oil phase
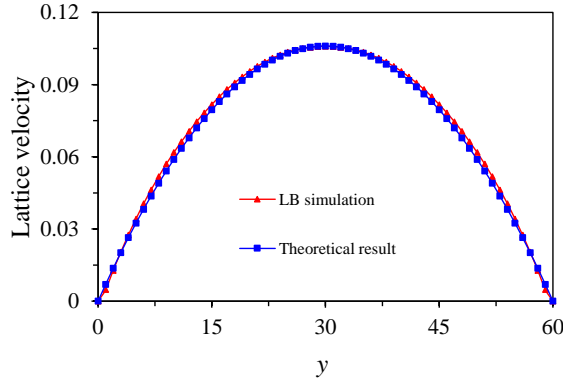
Fig. 2. Fitting result for oil velocity profile with the theoretical value at $x = 390$ (dimensionless).

velocity profile from the LB model:

$$\mathbf{u}(y) = \frac{1}{2\mu}y(H-y)\frac{\Delta P}{L} \quad (4)$$

$$Q = 2\int_0^H \mathbf{u}(y)dy = \frac{2H^3}{3\mu}\frac{\Delta P}{L} \quad (5)$$

where $\Delta P/L$ represents the pressure gradient, Pa/m, which is the required viscous force ΔP_v, y represents the location in the y axis, m, Q represents the flux, m²/s, H represents the width, m, μ denotes the dynamic viscosity, Pa·s.

Firstly, it is considered that the physical viscosity corresponds to the lattice viscosity and the relaxation time in the oil phase. By adjusting the pressure gradient in the HP equation, the velocity profile acquired from the LB model is fitted. The calculation process of the viscous force ΔP_v is as follows:

The oil phase velocity profile near the outlet ($x = 390$) is used to fit the HP equation to obtain the viscous force ΔP_v. The fitting example is shown in Fig. 2. The blue curve is drawn by the HP equation by adjusting the pressure gradient, and the red one is the simulation result obtained by the three-phase flow simulation model at $x = 390$. The results of the theoretical formula and the simulation are consistent. In the subsequent analysis, all of the viscous forces ΔP_v are estimated as mentioned above.

2.3 Physical background

The simulation is based on a factual oil reservoir in Sinopec Shengli Oilfield in China. The data on pore-throat structure in the target field are listed in Table 1.

3. Lattice Boltzmann model

3.1 Shan-Chen LB model for multiphase multicomponent flow

The LB model consists of a migration step and a collision step, where the migration step represents the migration process of the particles, and the collision step represents a relaxation process of the particle distribution function to the equilibrium state.

The average pore aperture for simulation is 0.6 μm, which equals 100 lattice unit spaces herein. The corresponding relation is shown in Table 2.

Table 1. Data of pore-throat structure in the target field.

Well number	Position	Average aperture (μm)
G1	First group	0.0286
	Second group	0.563
F2	First group	0.295
F3	Second group	0.539
F	First group	0.103
	Second group	0.168

A single relaxation time LB model is utilized to analyze the balance between capillary and viscous forces during CO_2 flooding in tight reservoirs. There is a set of particle distribution functions to capture fluid flow. Based on the simple and popular Bhatnagar-Gross-Krook (BGK) collision operator (Bhatnagar et al., 1954), the evolution of the LB equation is written as:

$$f_i^k(x+\mathbf{e}_i\Delta t, t+\Delta t) - f_i^k(x,t) = \\ -\frac{1}{\tau_k}[f_i^k(x,t) - f_i^{eq,k}(\rho_k,\mathbf{u}_k^{eq})] + \Delta t\mathbf{F}_i^k \quad (6)$$

where $f_i^k(x,t)$ represents the density distribution function of component k at the lattice site x and time t, $f_i^{eq,k}$ represents the equilibrium distribution function of component k, the lattice speed c relates to the lattice spacing Δx and the time step Δt, and τ_k is the dimensionless relaxation time for component k, which relates to the viscosity of a fluid v_k, and $v_k = c_s^2(\tau_k - 0.5)\Delta t$. The force term $\mathbf{F}_i^k$ is described in the following in the details. The discrete velocities $\mathbf{e}_i$ depend on the particular velocity model. Due to the adopted two-dimensional model, the D2Q9 model is selected for fluid flow. The corresponding discrete velocities $\mathbf{e}_i$ are given by:

$$\mathbf{e}_i = \begin{cases} (0,0) & i = 0 \\ c(\cos[(i-1)\frac{\pi}{2}], \sin[(i-1)\frac{\pi}{2}]) & i = 1, 2, 3, 4 \\ \sqrt{2}c(\cos[(2i-1)\frac{\pi}{4}], \sin[(2i-1)\frac{\pi}{4}]) & i = 5, 6, 7, 8 \end{cases} \quad (7)$$

The equilibrium distribution functions $f_i^{eq,k}$ for oil, scCO₂ and water phases in the D2Q9 model can be described by:

$$f_i^{eq,k} = w_i\rho_k\left[1 + \frac{\mathbf{e}_i\cdot\mathbf{u}_k^{eq}}{c_s^2} + \frac{(\mathbf{e}_i\cdot\mathbf{u}_k^{eq})^2}{2c_s^4} - \frac{\mathbf{u}_k^{eq^2}}{2c_s^2}\right] \quad (8)$$

In the above formula, w_i represent the weight coefficient in the corresponding directions, which are given by $w_i = 4/9$, $i = 0$; $w_i = 1/9$, $i = 1, 2, 3, 4$; $w_i = 1/36$, $i = 5, 6, 7, 8$.

The fluid density and velocity are calculated by:

$$\rho = \Sigma_i f_i \quad (9)$$

$$\mathbf{u} = \Sigma_i \mathbf{e}_i\frac{f_i}{\rho} \quad (10)$$

Based on the Chapman-Enskog expansion, the LB evolution equation (Eq. (6)) proves that it can recover the correct continuity (Eq. (1)) and momentum equations (Eq. (2)) by the

Table 2. Corresponding relation between the physical unit and the lattice unit.

Lattice number	Pore-throat aperture (μm)
60	0.36
80	0.48
100	0.6
120	0.72
140	0.84
160	0.96

Navier-Stokes equation (Chen et al., 1992; Qian et al., 1992).

The Shan-Chen LB model, also known as the pseudopotential model (Shan and Chen, 1993, 1994), mainly introduces attractive and repulsive forces through the interaction potential between particles, and is mostly used to simulate single-component multiphase flow and multicomponent multiphase flow. Subsequently, Shan and Doolen (1995) improved the Shan-Chen LB model by using modified velocity, considering the force term $\mathbf{F}_i^k$ on equilibrium velocity $\mathbf{u}_k^{eq}$:

$$\mathbf{u}_k^{eq} = \mathbf{u}_c + \tau_k \frac{(\mathbf{F}_{int,k,i} + \mathbf{F}_{ads,k,i})}{\rho_k} \qquad (11)$$

where $\mathbf{u}_c$ denotes the composite macroscopic velocity; $\mathbf{F}_{int,k,i}$ denotes the liquid-liquid interaction force; $\mathbf{F}_{ads,k,i}$ is the liquid-solid interaction force.

In the Shan-Chen LB model, these can be represented as:

$$\mathbf{u}_c = \frac{\sum_k \sum_i \frac{\mathbf{e}_i f_i}{\tau_k}}{\sum_k \frac{\rho_k}{\tau_k}} \qquad (12)$$

$$\mathbf{F}_{int,k,i}(x,t) = -\rho_k(x,t)G_{k\bar{k}}\sum_i w_i \rho_{\bar{k}}(x+\mathbf{e}_i\Delta t)\mathbf{e}_i \qquad (13)$$

$$\mathbf{F}_{ads,k,i}(x,t) = -\rho_k(x,t)G_{ks}\sum_i w_i s(x+\mathbf{e}_i\Delta t)\mathbf{e}_i \qquad (14)$$

where $G_{k\bar{k}}$ represents the liquid-liquid force parameter, and G_{ks} is the liquid-solid force parameter.

Compared with the oil-water two-phase Shan-Chen LB model, the main difference in the oil-gas-water three-phase Shan-Chen LB theoretical model is the calculation of the interaction forces between the oil-gas-water phases. In the three-phase model, the formulas for calculating the interaction forces among the three phases are:

$$\mathbf{F}_{A,i}(x,y) = -\psi_A(x)[G_{AA}\sum_i w_i \psi_A(x+\mathbf{e}_i\Delta t)\mathbf{e}_i +$$
$$G_{AB}\sum_i w_i \psi_B(x+\mathbf{e}_i\Delta t)\mathbf{e}_i + \qquad (15)$$
$$G_{AC}\sum_i w_i \psi_C(x+\mathbf{e}_i\Delta t)\mathbf{e}_i]$$

$$\mathbf{F}_{B,i}(x,y) = -\psi_B(x)[G_{BB}\sum_i w_i \psi_B(x+\mathbf{e}_i\Delta t)\mathbf{e}_i +$$
$$G_{BA}\sum_i w_i \psi_A(x+\mathbf{e}_i\Delta t)\mathbf{e}_i + \qquad (16)$$
$$G_{BC}\sum_i w_i \psi_C(x+\mathbf{e}_i\Delta t)\mathbf{e}_i]$$

$$\mathbf{F}_{C,i}(x,y) = -\psi_C(x)[G_{CC}\sum_i w_i \psi_C(x+\mathbf{e}_i\Delta t)\mathbf{e}_i +$$
$$G_{CA}\sum_i w_i \psi_A(x+\mathbf{e}_i\Delta t)\mathbf{e}_i + \qquad (17)$$
$$G_{CB}\sum_i w_i \psi_B(x+\mathbf{e}_i\Delta t)\mathbf{e}_i]$$

where $\psi(x)$ represents the effective mass or the pseudopotential, which is defined as $\psi_k(\rho_k) = 1 - \exp(-\rho_k)$ in this study.

The interaction strength between different components can be adjusted by G (Wang et al., 2022a, 2022b).

3.2 Boundary conditions

In this study, the non-equilibrium extrapolation method (Guo et al., 2002) is adopted to impose the velocity boundary condition at the inlet, realizing the displacement fluid injection at a constant velocity. Commonly, the distribution function $f_i^k(x,t)$ can be decomposed into the equilibrium and the non-equilibrium parts:

$$f_i^k(x,t) = f_i^{eq,k}(x,t) + f_i^{neq,k}(x,t) \qquad (18)$$

where $f_i^{eq,k}(x,t)$ and $f_i^{neq,k}(x,t)$ represent the equilibrium and the non-equilibrium parts, respectively. For the velocity boundary condition, the velocity $\mathbf{u}(O,t)$ at O is known while its density $\rho(O,t)$ is unknown, and the equilibrium distribution function is approximately obtained as:

$$f_i^{eq,k}(O,t) = f_i^{eq,k}(\rho(B,t), \mathbf{u}(O,t)) \qquad (19)$$

where $f_i^{eq,k}$ is adopted by Eq. (8), and the distribution function of $f_i^k(B,t)$, macroscopic density $\rho(B,t)$ and macroscopic velocity $\mathbf{u}(B,t)$ at B are known. Meanwhile, there exists a relationship of the non-equilibrium distribution functions between O and B:

$$f_i^{neq,k}(B,t) = f_i^{neq,k}(O,t) + O(\delta_x^2) \qquad (20)$$

In summary, the distribution function of $f_i^k(O,t)$ at O is given as:

$$f_i^k(O,t) = f_i^{eq,k}(O,t) + [f_i^k(B,t) - f_i^{eq,k}(B,t)] \qquad (21)$$

In turn, the fully-developed boundary condition is adopted at the outlet. Except for the inlet and outlet, the other wall surfaces with the no-slip boundary condition utilize the bounce-back boundary condition (Ziegler, 1993) in the LB model.

3.3 Numerical procedure

After initialization, each iteration contains the following substeps: (1) operating the streaming step; (2) obtaining the unknown distribution function by the default boundary condition; (3) calculating the interaction forces by the Shan-Chen LB model; (4) obtaining the macroscopic physical quantity; (5) operating the collision step. By repeating the above steps until a steady state, the simulation can be ceased and the required results are output.

3.4 Validation

3.4.1 Equilibrium contact angle

In order to verify the rationality of the multiphase multicomponent simulation model, the contact angle test of the model demonstrates that the model can simulate the interaction forces between the fluids and the wall to achieve different wettability conditions. The viscosity ratio of oil, water and gas is set to 5:3:1, and this relationship is used in subsequent simulations throughout this article. In this study, the viscosity of water in the lattice unit is 0.15, corresponding to 1E-06 m²/s in the physical unit. As can be seen from Fig. 3, by adjusting
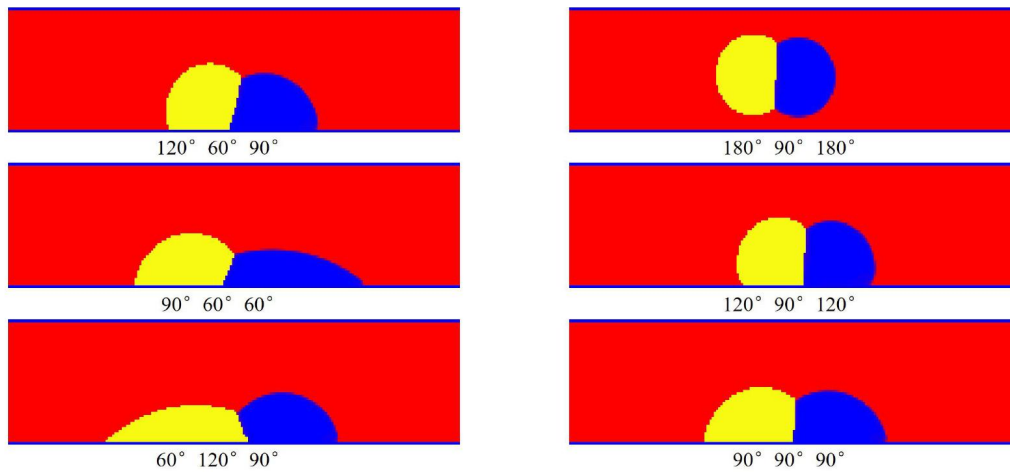
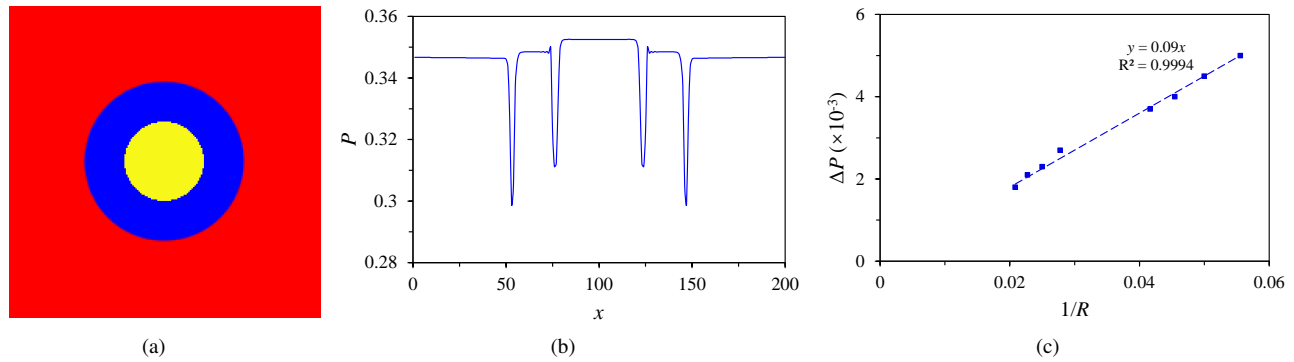**Fig. 3**. Contact angles of the three phases.

Fig. 4. (a) Numerical setup of Laplace's law, (b) pressure distribution along the x axis and (c) Laplace's law validation (dimensionless).

the value of the interaction force G_{ks} between the phases and the wall, the change of the contact angle from 0° to 180° can be achieved simultaneously.

The three phases are set as the external oil phase (red), gas phase (yellow), and water phase (blue), respectively. The contact angles used in the simulation are the water-wet contact angle of 60°, the neutral contact angle of 90°, and the oil-wet contact angle of 120°.

3.4.2 Laplace's law

Here, Laplace's law for IFT is carried out for the verification of the three-phase Shan-Chen LB model. It can be known from Laplace's law that $\Delta P = P_o - P_i = \sigma/R$, where P_o and P_i represent the pressure of the external phase and the internal phase, respectively, σ represents IFT, and R is the radius of the inner phase. The grid size is 200×200 lattices. Fig. 4(a) is the three-phase distribution diagram, in which the red is the oil phase, the blue is the water phase, and the yellow is the gas phase. The radius of the water phase R_w is the doubled one of the gas phase R_g.

The pressure difference ΔP is calculated under four different radii of the gas phase R_g (18, 20, 22, and 24), and the results are shown in Fig. 4(c). After fitting, a theoretical curve ($y = 0.09x$) can be obtained to describe the linear relation

between the droplet pressure difference and the reciprocal of the droplet radius. The variance R^2 for the fitting curve is 0.994, which indicates that the model is reasonable.

4. Simulation results and analysis

4.1 Calculation process of mechanical equilibrium

As described in section 2.2, the no-slip HP equation is used for the quantitative estimation of viscous force, and then to indirectly obtain the capillary force. First, the simulation result of the velocity profile from the model is acquired before the outflow of the oil phase. Then, the simulation result is fitted with the theoretical one. Finally, the viscous force is obtained by the no-slip HP equation of the pressure gradient term. If the viscous force increases under certain conditions, this means that the capillary force decreases simultaneously according to Eq. (3) under a constant total driving force.

4.2 Comparison of different displacement patterns in the single throat

In this part, four factors, namely, pore aperture, wettability, IFT between oil and water, and miscibility between oil and scCO$_2$, are discussed together to analyze their
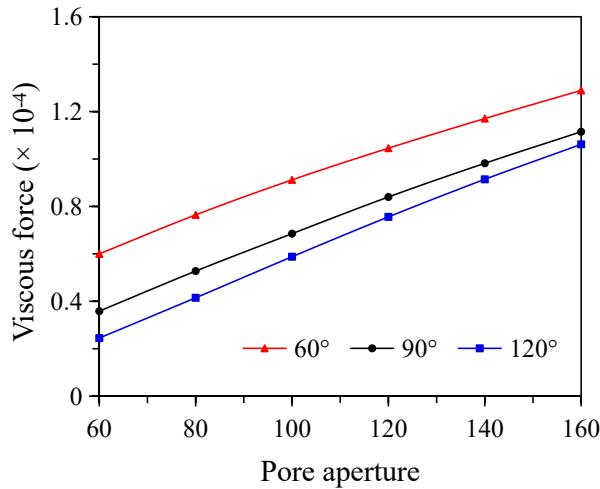
Fig. 5. Variation in viscous force with pore sizes under different contact angles (dimensionless).

Fig. 6. Variation in viscous force with pore sizes under different contact angles (dimensionless).

impact on the balance between capillary force and viscous force in the single throat. The schematic design is described below.

For the different pore apertures, the size of the computational domain is $400 \times H$, and the width H is varied from 60 to 160. The water wettability of the wall surface ranges from $60°$ to $120°$. For IFT, the interaction between oil and water is from high IFT to low IFT. For miscibility, the interaction strength between oil and $scCO_2$ is also from high to low.

4.2.1 Water flooding

Although the velocity boundary condition is adopted in this model, when calculating the viscous force, the conversion changes the constant velocity to constant pressure on displacement to guarantee the constant total driving force. According to the balance relation in Eq. (3), the viscous force increases under a lower contact angle and increment of pore aperture, which means that the capillary force drops under those conditions. The viscous force increases with the decrease in IFT, because the lower IFT reduces the capillary resistance, although IFT has a negligible effect on the capillary force for water flooding. It is shown in Fig. 5 that the viscous force is the largest in the water-wet ($60°$) pores. The reason is that the capillary force of the water-wet pores becomes resistance under the displacement condition, while the capillary force itself comprises the resistance in the oil-wet ($120°$) pores. This capillary resistance is greater than that in the water-wet condition, such that the displacing front moves faster in the water-wet pore.

4.2.2 ScCO₂ flooding

The water flooding front of the small hole reaches the exit first, that is, the smaller the diameter of the hole, the faster the movement of displacing front. By comparing the leading edges of the water and CO_2 flooding, it can be seen that the CO_2 flowing speed is faster because the miscible mechanism reduces the capillary resistance. The higher degree of oil-gas miscibility, namely, the smaller G value, causes CO_2 to be
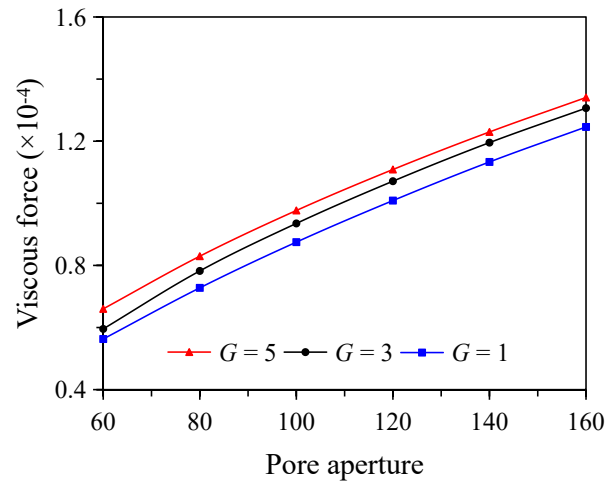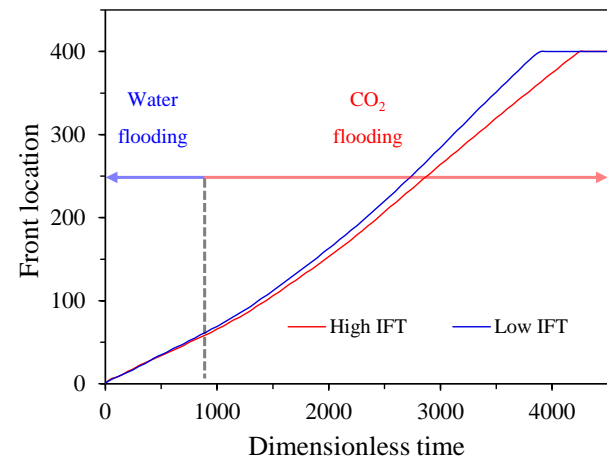

Fig. 7. Displacing front of CO_2 flooding after water flooding with the dimensionless time (dimensionless).

fully miscible with the oil phase and decreases the CO_2 concentration at the front. Then, the viscous force decreases, leading to the slower movement of the displacing front (Fig. 6).

Because the capillary resistance in the oil-wet pores is greater than that in the water-wet pores, resulting in a decrease in the viscous force of the system, the moving speed of the leading edge decreases gradually with the increase in the contact angle.

4.2.3 ScCO₂ flooding after water flooding

The increment of oil-water IFT leads to an increase in capillary resistance and a decrease in viscous force. After water injection (dimensionless time = 1,000) the displacing front moving speed slightly increases, because $scCO_2$ has a lower IFT with the oil than water and thus readily diffuses into the oil (Fig. 7).

In the case of CO_2 flooding after water flooding, the miscibility variation has little effect on the viscous force. The reason is that, although CO_2 can diffuse into the crude oil, it
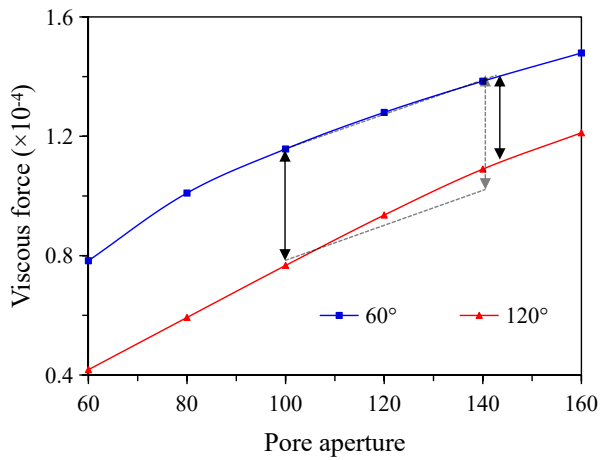
Fig. 8. Variation in viscous force with pore sizes under different contact angles (dimensionless).

Table 3. E_d value under water flooding.

Grid size	$E_d(\%)$		
	Water-wet	Oil-wet	Low IFT
200×200	88.99	77.39	94.76
300×300	84.47	77.46	92.16

is difficult to achieve gas breakthrough under the blocking of the water slug, therefore, the front moving speed remains unchanged.

Due to the smaller capillary resistance in the water-wet pores, the viscous force is greater than that in the oil-wet pores, and the difference will be magnified with the decreasing pore size. The oil-wet displacing front moves at a slower speed. Under the same conditions, the crude oil in the oil-wet reservoir is more difficult to be displaced. For the comparison of different wettability conditions, the smaller the pore diameter, the greater the change in viscous force, resulting in a more significant influence on the capillary force (Fig. 8).

4.3 Evaluation of EOR in the homogenous porous media

In this part, EOR estimation in the homogenous porous media is carried out by comparing the different displacement patterns mentioned above. Two sizes of the conceptual model are adopted: 200×200 and 300×300. The displacement efficiency (E_d) is given as:

$$E_d = \frac{\text{Initial oil} - \text{Residual oil after displacement}}{\text{Initial oil}} \quad (22)$$

4.3.1 Water flooding

Here, we analyze the wettability and IFT for water flooding, and the results are shown in Table 3. When horizontally comparing the different sizes of the computational domain, although the capillary force of the small-scale model is large, the viscous force is large when the total displacement force is high. Therefore, the oil displacement efficiency of the large-

Table 4. E_d value under scCO$_2$ flooding.

Grid size	$E_d(\%)$		
	Water-wet	Oil-wet	High miscibility
200×200	77.90	74.61	76.04
300×300	72.38	70.69	70.08

Table 5. E_d value under scCO$_2$ flooding after water flooding.

Grid size	$E_d(\%)$			
	Water-wet	Oil-wet	Low IFT	High miscibility
200×200	78.48	71.06	80.93	77.60
300×300	71.55	68.04	76.81	70.31

scale model is lower than that of the small model in the cases of the influencing factors of the water-wet wall and the low IFT. Based on the longitudinal comparison of the different influencing factors, if the oil-water IFT is reduced, the capillary force will plunge. The viscous force used for the displacement will then increase and the final displacement efficiency will also rise. The capillary resistance under the water-wet condition is smaller than that for the oil-wet surface, therefore, the displacement efficiency will plummet under the oil-wet condition.

4.3.2 ScCO$_2$ flooding

Wettability and miscibility are analyzed in this section under scCO$_2$ flooding, and the results are shown in Table 4. In the horizontal comparison, the large-scale model and the small-scale model are consistent with the conclusions obtained by water flooding in terms of water and oil wetness. The oil-wet wall surface attracts the crude oil, thereby increasing the displacement resistance and reducing the displacement efficiency. For a high degree of miscibility, the displacement efficiency is reduced because of the low oil-gas interaction force, and the dissolution of scCO$_2$ into the oil reduces the gas density and the fluid rate, which is consistent with the conclusions obtained by scCO$_2$ flooding in the single throat.

4.3.3 ScCO$_2$ flooding after water flooding

Wettability, IFT and miscibility are analyzed in this part for the pattern of scCO$_2$ flooding after water flooding (Fig. 9), and the results are shown in Table 5. When comparing horizontally, the large-scale model and the small-scale model are consistent with the conclusions obtained by the patterns of water flooding and scCO$_2$ flooding in terms of water-wet and oil-wet walls, low IFT, and high miscibility. From the perspective of displacement efficiency, the order of the three displacement patterns is water flooding > scCO$_2$ flooding > water flooding followed by scCO$_2$ flooding, which is consistent with the front moving speed of the different displacement patterns in the single throat. The faster the movement of the displacing front, the higher the final displacement efficiency.
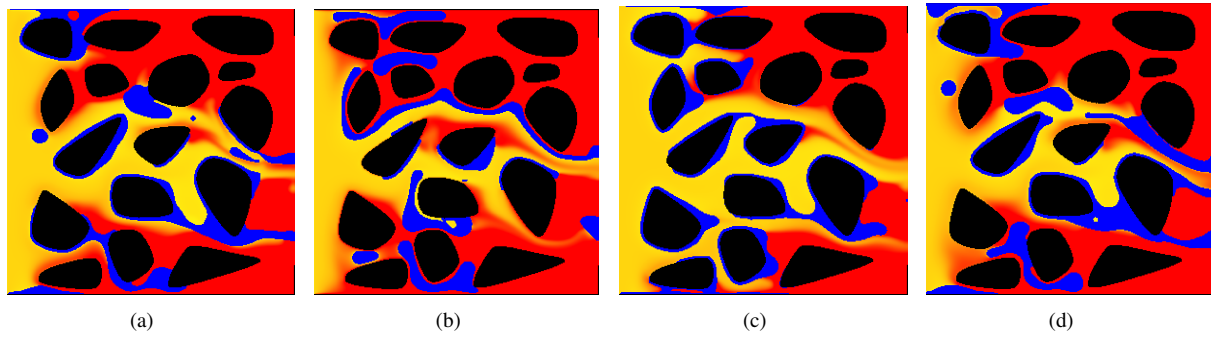
Fig. 9. Diagram for scCO$_2$ flooding after water flooding in the homogenous porous media, (a) water-wet condition, (b) oil-wet condition, (c) low IFT condition and (d) high miscibility condition.
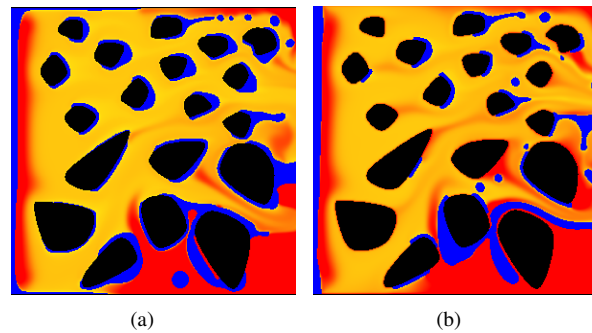

Fig. 10. Diagram for WAG under different wettability conditions in heterogeneous porous media, (a) water-wet condition and (b) oil-wet condition.

Table 6. E_d value under three displacement patterns.

Wettability	Grid size	$E_d(\%)$		
		scCO$_2$ flooding	Water before scCO$_2$	WAG
Water-wet	200×200	78.79	80.66	79.09
	300×300	76.60	76.27	81.58
Oil-wet	200×200	77.84	75.37	80.99
	300×300	75.70	71.96	77.34

4.4 Effects of heterogeneity and displacement patterns on EOR

Similar to the above, the displacement patterns in 4.3 are used to analyze EOR for the heterogeneous porous media, and the permeability ratio between the upper and lower parts in the main porous medium is 1.38 according to the single-phase calculations (Fig. 10), and E_d is also calculated by Eq. (22). The three displacement patterns of E_d are listed in Table 6. For the comparison of computational size, although the capillary force of the small-scale model is large, the viscous force is high when the total displacement force is large. Therefore, the displacement efficiency of the large-scale model is lower than that of the small-scale model under the influencing factors of water-wet and oil-wet conditions. Under the wettability

comparison, the capillary resistance under water-wet condition is smaller than the oil-wet capillary force, i.e., it is the resistance itself, therefore, the oil-wet viscous force is greatly reduced according to Eq. (3). The impact of wettability on scCO$_2$ flooding after water flooding is greater than that under continuous scCO$_2$ flooding because the capillary force of water is smaller than that of scCO$_2$ under the water-wet condition, which is more conducive to displacement.

When comparing the three displacement patterns, it can be seen that the magnitude of displacement efficiency from large to small is WAG > scCO$_2$ flooding after water flooding > continuous scCO$_2$ flooding. Due to the smaller viscosity and the higher miscibility, the front of scCO$_2$ moves slower, while the front of water moves faster, and the displacement distance is greater than that of scCO$_2$ in a same interval. The scCO$_2$ flooding after water flooding and WAG with the energy replenishment for displacement can not only spread to a larger area, but also increase the overall displacement efficiency.

5. Conclusions

In this study, a multiphase multicomponent Shan-Chen LB model is established to analyze the balance between capillary force and viscous force for EOR in tight reservoirs. The reasonability of the model is verified by contact angle test and Laplace's law. Single throat models are used to analyze the variation in capillary force under different injection fluids, displacement patterns, wettabilities, fluid properties (e.g.,

miscibility, IFT), and pore apertures. In addition, the heterogeneous and homogenous models are also built to explore the impact of the influencing factors mentioned above on EOR. The main findings of this study are as follows:

1) With the increment of pore aperture, miscibility, and the decrease in IFT, the capillary force will decline to different degrees, the corresponding results are quantified in this study. The oil-wet wall surface is adverse for both water and $scCO_2$ flooding.

2) Compared with water flooding, the leading edge of continuous CO_2 flooding, CO_2 flooding after water flooding, and WAG are much more sluggish due to the higher miscibility and the smaller viscosity. As for the performance of displacement efficiency, the order of different displacement patterns, from large to small, is WAG > $scCO_2$ flooding after water flooding > continuous $scCO_2$ flooding.

This study proposes a set of quantitative estimation methods to explore the impact of capillary force on EOR in tight reservoirs for a better understanding of the balance between capillary and viscous forces, and to provide guidance for field projects.

Acknowledgement

Conflict of interest

The authors declare no competing interest.

References

Alvarado, V., Manrique, E. Enhanced oil recovery: An update review. Energies, 2010, 3(9): 1529-1575.

Bhatnagar, P. L., Gross, E. P., Krook, M. A model for collision processes in gases. I. Small amplitude processes in charged and neutral one-component systems. Physical Review, 1954, 94(3): 511-525.

Cai, J., Jin, T., Kou, J., et al. Lucas-Washburn equation-based modeling of capillary-driven flow in porous systems. Langmuir, 2021, 37(5): 1623-1636.

Cai, J., Yu, B., Mei, M., et al. Capillary rise in a single tortuous capillary. Chinese Physics Letters, 2010, 27(5): 054701.

Chen, H., Chen, S., Matthaeus, W. H. Recovery of the Navier-Stokes equations using a lattice-gas Boltzmann method. Physical Review A, 1992, 45(8): R5339-R5342.

Christensen, J. R., Stenby, E. H., Skauge, A. Review of WAG field experience. SPE Reservoir Evaluation & Engineering, 2001, 4(2): 97-106.

Dong, B., Yan, Y., Li, W. LBM simulation of viscous fingering phenomenon in immiscible displacement of two fluids in porous media. Transport in Porous Media, 2011, 88(2): 293-314.

Ghedan, S. G. Global laboratory experience of CO_2-EOR flooding. Paper SPE 125581 Presented at the SPE/EAGE Reservoir Characterization and Simulation Conference, Abu Dhabi, UAE, 19-21 October, 2009.

Guo, Z., Zheng, C., Shi, B. Non-equilibrium extrapolation method for velocity and pressure boundary conditions in the lattice Boltzmann method. Chinese Physics, 2002, 11(4): 366-374.

Jarrell, P. M., Fox, C. E., Stein, M. H., et al. Practical Aspects of CO_2 Flooding. Richardson, USA, Society of Petroleum Engineers, 2002.

Jensen, M. D., Pei, P., Snyder, A. C., et al. Methodology for phased development of a hypothetical pipeline network for CO_2 transport during carbon capture, utilization, and storage. Energy & Fuels, 2013, 27(8): 4175-4182.

Jiang, J., Rui, Z., Hazlett, R., et al. An integrated technical-economic model for evaluating CO_2 enhanced oil recovery development. Applied Energy, 2019, 247: 190-211.

Khosravi, M., Bahramian, A., Emadi, M., et al. Mechanistic investigation of bypassed-oil recovery during CO_2 injection in matrix and fracture. Fuel, 2014, 117: 43-49.

Lackner, K. S. A guide to CO_2 sequestration. Science, 2003, 300(5626): 1677-1678.

Lambert, M. R., Marino, S. D., Anthony, T. L., et al. Implementing CO_2 floods: No more delays! Paper SPE 35187 Presented at the Permian Basin Oil and Gas Recovery Conference, Midland, Texas, 27-29 March, 1996.

Landau, L. D., Lifshits, E. M. Fluid Mechanics. London, UK, Pergamon Press, 1959.

Lansangan, R. M., Smith, J. L. Viscosity, density, and composition measurements of CO_2/West Texas oil systems. SPE Reservoir Engineering, 1993, 8(3): 175-182.

Lenormand, R., Zarcone, C., Sarr, A. Mechanisms of the displacement of one fluid by another in a network of capillary ducts. Journal of Fluid Mechanics, 1983, 135: 337-353.

Liu, Y., Berg, S., Ju, Y., et al. Systematic investigation of corner flow impact in forced imbibition. Water Resources Research, 2022, 58(10): e2022WR032402.

Martin, D. F., Taber, J. J. Carbon dioxide flooding. Journal of Petroleum Technology, 1992, 44(4): 396-400.

Nobakht, M., Moghadam, S., Gu, Y. Effects of viscous and capillary forces on CO_2 enhanced oil recovery under reservoir conditions. Energy & Fuels, 2007, 21(6): 3469-3476.

Qian, Y. H., d'Humières, D., Lallemand, P. Lattice BGK models for Navier-Stokes equation. Europhysics Letters, 1992, 17(6): 479-484.

Rao, D. N., Girard, M., Sayegh, S. G. Impact of miscible flooding on wettability, relative permeability, and oil recovery. SPE Reservoir Engineering, 1992, 7(2): 204-212.

Salama, A., Cai, J., Kou, J., et al. Investigation of the dynamics of immiscible displacement of a ganglion in capillaries. Capillarity, 2021, 4(2): 31-44.

Shan, X., Chen, H. Lattice Boltzmann model for simulating flows with multiple phases and components. Physical Review E, 1993, 47(3): 1815-1819.

Shan, X., Chen, H. Simulation of nonideal gases and liquid-gas phase transitions by the lattice Boltzmann equation. Physical Review E, 1994, 49(4): 2941-2948.

Shan, X., Doolen, G. Multicomponent lattice-Boltzmann model with interparticle interaction. Journal of Statistical Physics, 1995, 81(1): 379-393.

Tang, G., Morrow, N. R. Influence of brine composition and fines migration on crude oil/brine/rock interactions and oil recovery. Journal of Petroleum Science and Engineering, 1999, 24(2-4): 99-111.

Tapia, J. F. D., Lee, J. Y., Ooi, R. E. H., et al. Optimal CO_2 allocation and scheduling in enhanced oil recovery (EOR) operations. Applied Energy, 2016, 184: 337-345.

Tsuji, T., Jiang, F., Christensen, K. T. Characterization of immiscible fluid displacement processes with various capillary numbers and viscosity ratios in 3D natural sandstone. Advances in Water Resources, 2016, 95: 3-15.

Wang, S., Chen, S., Li, Z. Characterization of produced and residual oils in the CO_2 flooding process. Energy & Fuels, 2016, 30(1): 54-62.

Wang, G., Liao, R., Li, J. The development situation and future of low permeability oil reservoirs of SINOPEC. Petroleum Geology and Recovery Efficiency, 2007, 14(3): 84-89. (in Chinese)

Wang, H., Su, Y., Wang, W., et al. CO_2-oil diffusion, adsorption and miscible flow in nanoporous media from pore-scale perspectives. Chemical Engineering Journal, 2022a, 450: 137957.

Wang, H., Wang, W., Su, Y., et al. Lattice Boltzmann model for oil/water two-phase flow in nanoporous media considering heterogeneous viscosity, liquid/solid, and liquid/liquid slip. SPE Journal, 2022b: 210564.

Wei, B., Zhang, X., Liu, J., et al. Adsorptive behaviors of supercritical CO_2 in tight porous media and triggered chemical reactions with rock minerals during CO_2-EOR and sequestration. Chemical Engineering Journal, 2020, 381: 122577.

Welkenhuysen, K., Rupert, J., Compernolle, T., et al. Considering economic and geological uncertainty in the simulation of realistic investment decisions for CO_2-EOR projects in the North Sea. Applied Energy, 2017, 185: 745-761.

Xiao, Y., He, Y., Zheng, J., et al. Modeling of two-phase flow in heterogeneous wet porous media. Capillarity, 2022, 5(3): 41-50.

Xu, T., Tian, H., Zhu, H., et al. China actively promotes CO_2 capture, utilization and storage research to achieve carbon peak and carbon neutrality. Advances in Geo-Energy Research, 2022, 6(1): 1-3.

Yousef, A. A., Al Saleh, S., Al Kaabi, A., et al. Laboratory investigation of the impact of injection-water salinity and ionic content on oil recovery from carbonate reservoirs. SPE Reservoir Evaluation & Engineering, 2011, 14(5): 578-593.

Zhang, L., Chen, L., Hu, R., et al. Subsurface multiphase reactive flow in geologic CO_2 storage: Key impact factors and characterization approaches. Advances in Geo-Energy Research, 2022, 6(3): 179-180.

Zhang, Y., Lashgari, H. R., Di, Y., et al. Capillary pressure effect on phase behavior of CO_2/hydrocarbons in unconventional reservoirs. Fuel, 2017, 197: 575-582.

Zhao, Y., Zhang, Y., Lei, X., et al. CO_2 flooding enhanced oil recovery evaluated using magnetic resonance imaging technique. Energy, 2020, 203: 117878.

Zhou, X., Chen D., Xia Y., et al. Spontaneous imbibition characteristics and influencing factors of Chang 7 shale oil reservoirs in Longdong area, Ordos basin. Earth Science, 2022, 47(8): 3045-3055. (in Chinese)

Ziegler, D. P. Boundary conditions for lattice Boltzmann simulations. Journal of Statistical Physics, 1993, 71(5): 1171-1177.